SUPPLEMENTARY MATERIAL

Rapid Synthesis of Defective and Composition-controlled Metal Chalcogenide Nanosheets by Supercritical Hydrothermal Processing

Yuta Nakayasu[a,*], Siobhan Bradley[b], Hiroaki Kobayashi[a], Keiichiro Nayuki[c], Yoshikazu Sasaki[c], Takaaki Tomai[a], Thomas Nann[d] and Itaru Honma [a,*]

a. IMRAM, Tohoku University, 2-1-1 Katahira, Aoba-ku, Sendai, Miyagi, 980-8577, Japan

b. ARC Centre of Excellence in Exciton Science, School of Chemistry, The University of Melbourne, Parkville, Victoria 3010, Australia

c Field Solution Division, JEOL Ltd., Tokyo 196-0022, Japan

d School of Mathematical and Physical Sciences, The University of Newcastle, Callaghan NSW 2308, Australia.

*Corresponding author: *nakayasu@tohoku.ac.jp, itaru.homma.e8@tohoku.ac.jp*

Tel: 022(217)5816; Fax: 022(217)5828

Total number of pages: 9

Total number of figures: 3

Total number of tables: 3

Table of Contents

Experimental method

Synthesis of TMDs

To compare the synthesized nanosheets with the bulk materials, bulk MoS_2, $MoS_{1.5}Se_{0.5}$, $MoS_{1.0}Se_{1.0}$, $MoS_{0.5}Se_{1.5,}$ and $MoSe_2$ (KOJUNDO CHEMICAL LABORATORY) were purchased. Before SCF chalcogenization, MoO_3 (Wako Chemicals) for preparing MoS_2, $MoSe_2$ and $Mo(S,Se)_2$, WO_3 (Wako Chemicals) for preparing WS_2, and a mixture of MoO_3 and WO_3 with the same molar ratio as $(Mo,W)S_2$ were ball milled for 4 h. To synthesize MoS_2, $Mo(S,Se)_2$, and $MoSe_2$, 1 mmol of ascorbic acid (Wako Chemicals) as a reducing agent was dissolved in 5 ml of water and the mixture was magnetically stirred for at least 20 min under ambient condition. Subsequently, S powder (Sigma-Aldrich), Se powder (Wako Chemicals) and ball-milled MoO_3 for preparing each product, were placed in a 10 ml, batch-type Hastelloy reactor in amounts as shown in Table S1. Lastly, 5 ml of the aqueous ascorbic acid solution was injected into the reactor vessels containing the powder mixture. The sealed reactor was kept at 400°C in a tube furnace for 30 min. After heating, the reactor was submerged in a water bath to terminate the reaction. The solution was separated by suction filtration, and the separated particles were dried under vacuum at room temperature. For synthesizing WS_2 and $(Mo,W)S_2$, S powder, ball-milled MoO_3 and ball-milled WO_3 were placed in the reactor in amounts as shown in Table S1. Then, 1 ml of formic acid (Wako Chemicals) as a reducing agent and 5 ml of water was injected into the reactor vessels containing the powders. The sealed reactor was kept at 400°C in a tube furnace for 60 min. After heating, the samples were collected in the same procedure as above. The difference of the recucing agents is caused by the difference of the redox potential as shown below.

$MoO_3 + 2H^+ + 2e \leftrightarrow MoO_2 + H_2O$ 0.227 V *vs* SHE[1]

$WO_3 + 2H^+ + 2e \leftrightarrow WO_2 + H_2O$ 0.036 V *vs* SHE[1]

Table S1 All quantities used for the preparation of each material

Source amount (mmol)	MoO_3	WO_3	S	Se
$MoSe_2$	0.30	-	-	0.70
$Mo(S,Se)_2$	0.30	-	0.30	0.70
MoS_2	0.30	-	1.0	-
$(Mo,W)S_2$	0.15	0.15	1.0	-
WS_2	-	0.30	1.0	-

Material characterization

The compositions of the synthesized TMD samples were analyzed using CHNS analysis (Elementar, vario EL cube) for sulfur and inductively coupled plasma-mass spectroscopy (ICP-MS; Agilent 8800) for the other elements. The crystal structure of the samples was analyzed using θ–2θ X-ray diffraction (XRD; Bruker AXS D8 Advance) using Cu-Kα radiation. To investigate the type and quality of chemical bonds and degree of crystallization, Raman spectroscopy was performed for MoS_2, $Mo(S,Se)_2$ using 514 nm wavelength laser excitation. X-ray photoelectron spectroscopy (XPS; PHI5000 VersaProbe II) was carried out to clarify the ionic valence of Mo and W. The grain size and morphology of the samples were observed using surface scanning electron microscopy (SEM; HITACHI SU6600) and transmission electron microscopy (TEM; Topcon EM-002B). Elemental mapping of $Mo(S,Se)_2$ and $(Mo,W)S_2$ was performed using scanning TEM coupled with energy dispersive X-ray spectroscopy (STEM-EDS; JEM-ARM200F) at an atomic level. Evaluation of compositional changes in $Mo(S,Se)_2$ and $(Mo,W)S_2$ was carried out using extended X-ray absorption fine structure (EXAFS) analysis at the Aichi Synchrotron Radiation Center.

For electrochemical characterization, 12 mg of TMD samples synthesized using SCW, and 6 mg of carbon black (Alfa Aesar) as a conductive agent were dissolved in 3 ml of water and 60 μL of Nafion solution (5 wt.%, Sigma-Aldrich). Then, the mixture was ultrasonicated for at least 10 min to prepare a catalyst ink. A glassy-carbon electrode was washed in ethanol for at least 30-min ultrasonication after polished by a cream containing aluminum. Then, 20 μL of the ink (containing 78 μg of catalyst) was loaded onto the glassy-carbon electrode with a diameter of 5 mm (catalyst loading ~0.40 mg/cm^2). The paste-dropped electrode left for over 1 hour for drying the ink. Linear sweep voltammetry (LSV) was carried out in the range from 0.2 V to -0.8V in a standard three-electrode configuration with a paste-dropped glassy-carbon electrode, a reversible hydrogen electrode (BAS Corporation, RHEK), and a platinum electrode as the working, reference, and counter electrodes, respectively, in a 0.5 M H_2SO_4 electrolyte solution. The values of the onset potential and overpotential were extracted from the LSV measurements for the 3rd and 224th cycles at a scan rate of 10 mV/s, while the Tafel slopes were derived from data from the 5th and 225th cycles measured at 5 mV/s. For cycles 5–223, a scan rate of 100 mV/s was used.

Table S2 XPS analysis for the synthesized samples.

XPS(ratio)	Mo 3d(IV)	Mo 3d(VI)	W 4f	S 2p	Se 3d
$MoSe_2$	1.12	-	-	-	1.88
$Mo(S,Se)_2$	0.98	0.06	-	1.39	0.57
MoS_2	1.03	0.02		1.95	-
$(Mo,W)S_2$	0.48	0.05	0.51	1.96	-
WS_2			1.02	1.98	-

Table S3 Elemental ratios of the samples and the mixture of ball-milled MoO_3 and WO_3 sources, where the Mo, W, and Se contents were determined using ICP-MS, and that of S was measured using CHNS analysis

ICP-MS/CHNS (ratio)	Mo	W	S	Se
$MoSe_2$	0.80	-	-	2.20
$Mo(S,Se)_2$	0.83	-	1.26	0.91
MoS_2	0.91	-	2.09	-
$(Mo,W)S_2$	0.58	0.63	1.79	-
WS_2	-	1.04	1.96	-

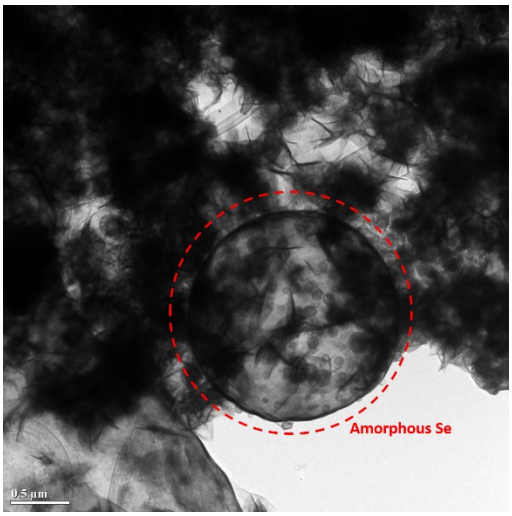

Fig. S1 A TEM image of synthesized $MoSe_2$. Amorphous Se is contaminated with synthesized $MoSe_2$.

ICP-MS and CHNS elemental analysis, and the results are shown in Table S3. The MoS_2 and WS_2 products showed almost stoichiometric compositions, while $Mo(S,Se)_2$ and $MoSe_2$ were rich in Se because of relatively Mo-poor composition. In contrast, XPS analysis indicated stoichiometric compositions for $Mo(S,Se)_2$ and $MoSe_2$ (Table S3), while EXAFS measurements indicated a S:Se ratio of around 1.4:0.6 (Fig. S3(b)). This indicates that pure amorphous selenium contaminated the samples. In fact, TEM image of $MoSe_2$ showed that amorphous Se was left in the sample as shown Fig. S1. As a future work, it is necessary to develop a method to completely remove the excess Se. However, the $(Mo,W)S_2$ composition was sulfur poor. According to previous reports,[2] insertion of molybdenum into WS_2 monolayers resulted in S vacancies. In our case, we assume that sulfur vacancies occurred in the layer plane.

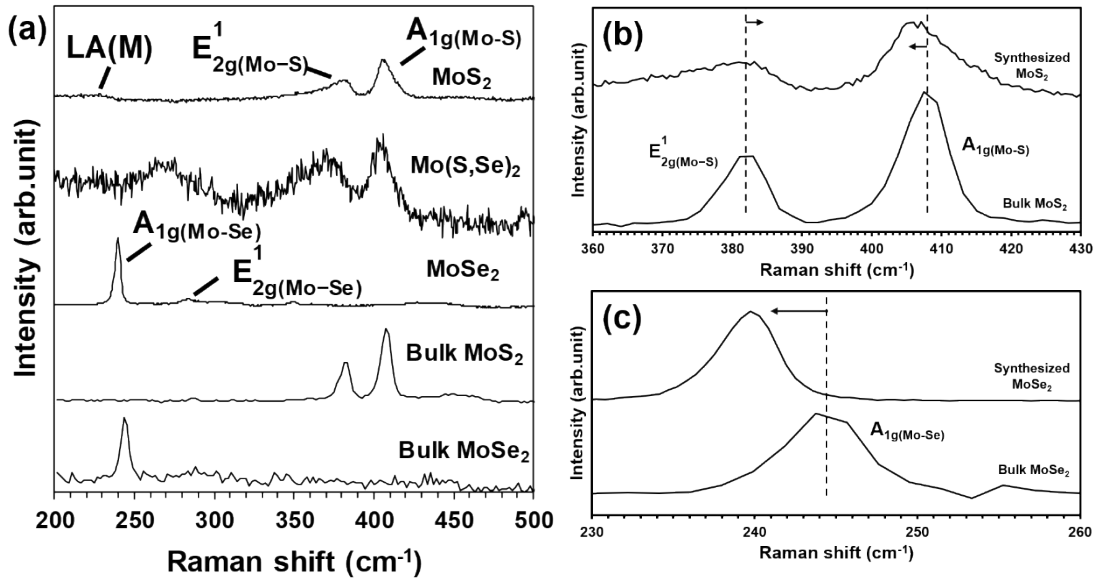

Fig. S2(a) Raman spectra analyses of synthesized $MoSe_2$, $Mo(S,Se)_2$, and MoS_2. Data for bulk commercial $MoSe_2$ and $MoSe_2$ are given for reference. (b) Comparison of synthesized MoS_2 with commercial one, and (c) Comparison of synthesized $MoSe_2$ with commercial one in A_{1g} mode.

Raman spectra for synthesized and commercial bulk $MoSe_2$, $Mo(S,Se)_2$, and MoS_2 are shown in Fig. S2(a). The in-plane E^1_{2g} and out-of-plane A_{1g} Raman vibration modes were around 385 and 406 cm^{-1}, respectively, for both synthesized and commercial MoS_2. In a previous report,[3] as MoS_2 was reduced to less than six layers, the spacing between the E^1_{2g} and A_{1g} peaks decreased. Here, the spacing between these peaks for the synthesized MoS_2 was narrower than that of the commercial sample, suggesting that few-layered MoS_2 was formed. In addition, the LA(M) mode was also detected although the peak intensity is low. The LA(M) mode in the Raman spectrum of MoS_2 around 227 cm^{-1} is known to acquire intensity in the presence of defects.[4] Hence, the synthesized MoS_2 has a defective structure.

The out-of-plane A_{1g} Raman vibration mode of the synthesized $MoSe_2$ was observed around 240 cm^{-1}, while that of commercial $MoSe_2$ was around 244 cm^{-1}; this redshift indicates a high monolayer content in the synthesized $MoSe_2$, consistent with a previous report.[5] Two sets of vibration modes were affected by the S and Se composition: Mo–S modes at high frequency (around 370 and 400 cm^{-1}) and Mo–Se modes at low frequency (around 225 and 275 cm^{-1}) in both the synthesized and commercial $Mo(S,Se)_2$. The addition of Se to MoS_2 resulted in both sets of vibration modes shifting to lower frequency, suggesting that mixing S and Se atoms resulted in the Mo–S and Mo–Se modes becoming weaker and decreasing in vibration frequency.

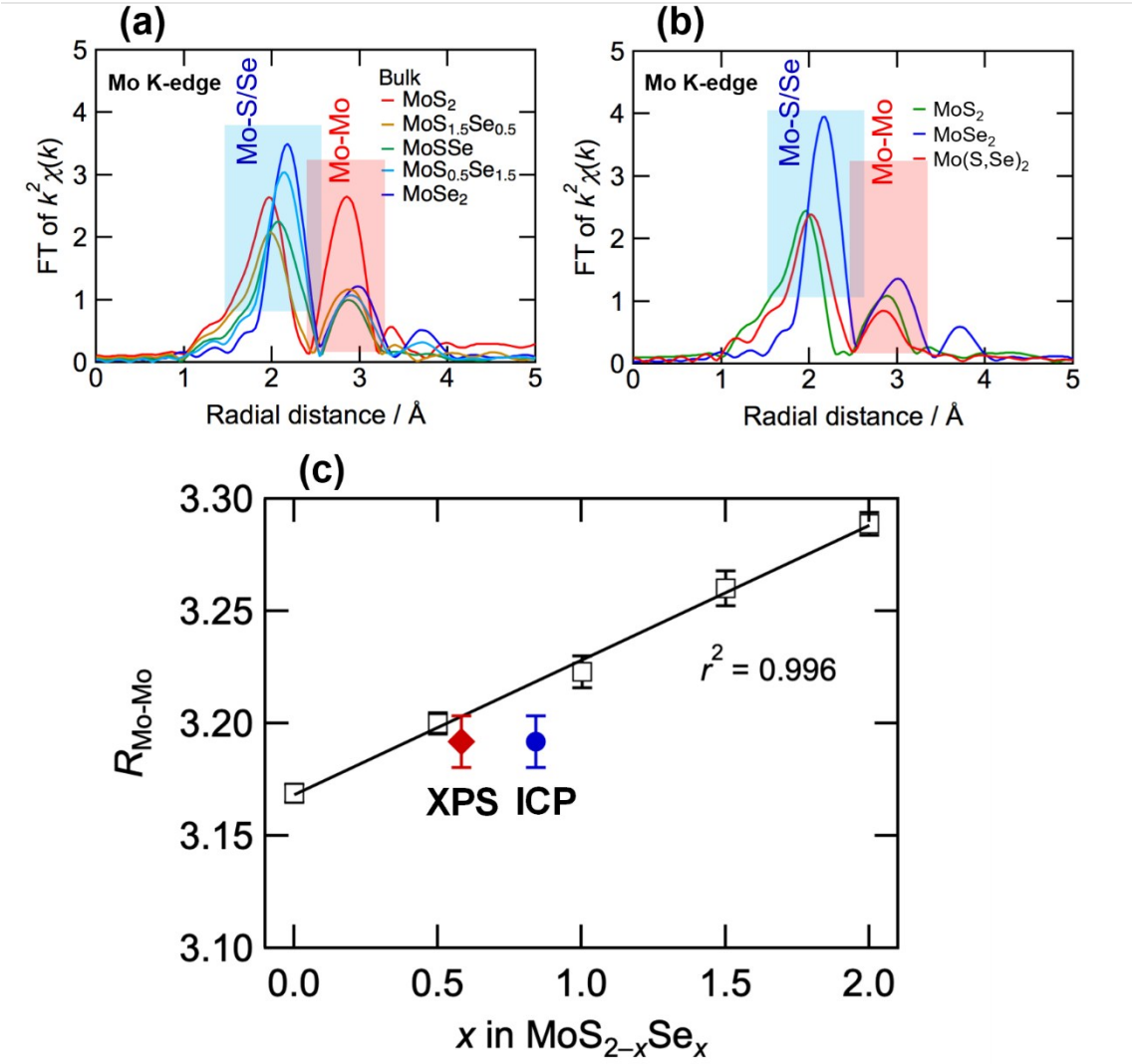

Fig. S3 Fourier-transformed k^2-weighted EXAFS data plotted as a radial structure function at the Mo *K*-edge. (a) Bulk MoS_2, $MoS_{1.5}Se_{0.5}$, $MoS_{1.0}Se_{1.0}$, $MoS_{0.5}Se_{1.5}$, and $MoSe_2$ (b) MoS_2, $Mo(S,Se)_2$, and $MoSe_2$ synthesized using the SCW process. (c) Bonding distance between Mo and Mo relative as a function of the chalcogen composition ratio of $MoS_{2-x}Se_x$

We carried out EXAFS measurements for bulk MoS_2, $MoS_{1.5}Se_{0.5}$, $MoS_{1.0}Se_{1.0}$, $MoS_{0.5}Se_{1.5}$, and $MoSe_2$, and synthesized MoS_2, $Mo(S,Se)_2$, and $MoSe_2$ as shown in Fig S3(a–c). In order to accurately determine the chalcogen composition of synthesized $Mo(S,Se)_2$, the bond distances between Mo and Mo derived from EXAFS data for the composition of bulk MoS_2, $MoS_{1.5}Se_{0.5}$, $MoS_{1.0}Se_{1.0}$, $MoS_{0.5}Se_{1.5}$, and $MoSe_2$ were plotted. The bonding distance was clearly proportional to the chalcogen composition ratio. The Mo–Mo distance in the synthesized $Mo(S,Se)_2$ was ~3.19 Å. The results of XPS and ICP agreed well with the XPS results. Therefore, the unexpected ICP results were attributed to contamination by amorphous Se, which results in a S:Se ratio in $Mo(S,Se)_2$ of 1.4:0.6.

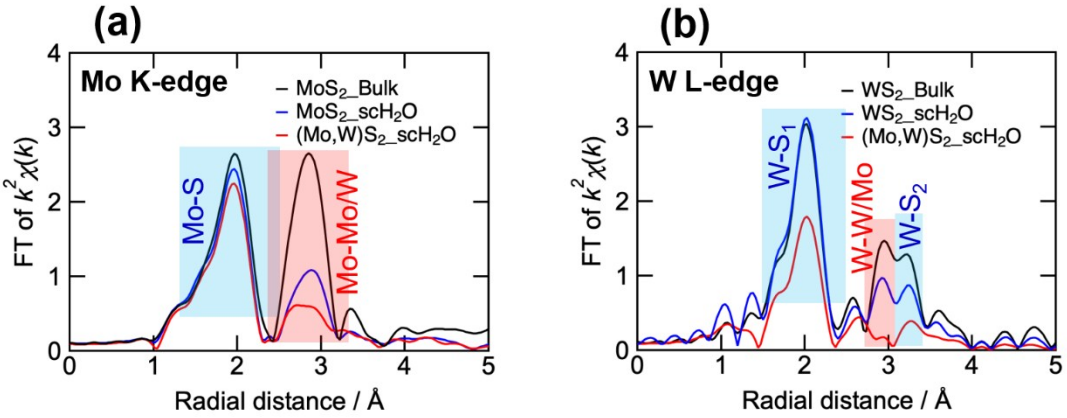

Fig. S4 Fourier-transformed k^2-weighted EXAFS data plotted as a radial structure function at the Mo *K*-edge and W *L*-edge. (a) Bulk MoS_2, and synthesized MoS_2 and $(Mo,W)S_2$. (b) Bulk WS_2, and synthesized MoS_2 and $(Mo,W)S_2$.

We carried out EXAFS measurements for bulk MoS_2 and WS_2, and synthesized MoS_2, $(Mo,W)S_2$, and WS_2 as shown in Fig. S4(a,b). The k^2 $\chi(k)$ signal of $(Mo,W)S_2$ was clearly different from those of pure MoS_2 and WS_2, indicating a remarkable change in the local atomic arrangement. As shown in Fig. S3(a), the Fourier transform (FT) curve of bulk MoS_2 was characterized by two main peaks, which were assigned to a S shell (1.9 Å) and a Mo shell (2.8 Å). In a previous report, the number of S edges in MoS_2 was quantitatively estimated using EXAFS.[6] The coordination number ratio between S and Mo (N_{Mo-S}/N_{Mo-Mo}) quantifies the number of sulfur edges in MoS_2, where edge-rich MoS_2 structures show higher coordination number ratios than bulk MoS_2.[6] The intensity of the N_{Mo-Mo} signal in MoS_2 synthesized by the SCW process was lower, while the N_{Mo-S}/N_{Mo-Mo} value was remarkably higher than those of the bulk sample; this indicates the change in the coordination number ratio. Therefore, the use of the SCW process is effective for synthesizing edge-rich structures. The FT curves of $(Mo,W)S_2$ shown in Fig. S4(a) show that the intensity of the two peaks decreased with respect to those of synthesized MoS_2 and bulk MoS_2, indicating the presence of defects introduced by the SCW process. In particular, the intensity derived from Mo–Mo(W) bonding was low. In the case that adjacent atoms are Mo, the two photoelectrons derived from Mo interfere with each other, whereas in case that adjacent atoms are Mo and W, the photoelectron derived from Mo does not interfere. Therefore, a favorable solid solution was formed.

Similarly, the FT curve of bulk WS_2 shown in Fig. S4(b) was characterized by three main peaks, which were assigned to sulfur shells (2.0 Å and 3.3 Å) and a tungsten shell (2.9 Å)[7,8]. The FT curves of $(Mo,W)S_2$ indicate that the intensity of all peaks decreased; in particular, the intensity derived from W–W(Mo) bonding was very low. This was due to the same reason described for the

Mo *K*-edge.

Table S4 HER activity compared with the state of the art electrodes synthesized by solvothermal or hydrothermal.

Materials	Overpotential [V] $(Mo,W)S_2$ @25mA/cm^2 $Mo(S,Se)_2$ @10mA/cm^2	Tafel slope [mV/dec]	Method	Reaction time
$Mo_{0.40}W_{0.60}S_2$ [9] $Mo_{0.67}W_{0.33}S_2$ [9]	>0.3 >0.3	117.8 114.4	Solvothermal	24 hr
Multi-walled carbon nanotubes @$Mo_{0.54}W_{0.46}S_2$ [10]	0.21	68	Hydrothermal	12 hr
$(Mo,W)S_2$ This study	0.27	70	Supercritical hydrothermal	60 min
$MoS_{1.34}Se_{0.66}$ [11]	0.17	55	Solvothermal	3.5 hr
$MoS_{1.5}Se_{0.5}$ [12]	0.18	43	Solvothermal	4 hr
$Mo(S,Se)_2$ This study	0.20	66	Supercritical hydrothermal	30 min

References

[1] P. Vanýsek, CRC Handbook of Chemistry and Physics, 92th Edition.

[2] Azizi, A.; Wang, Y.; Stone, G.; Elías, A. L.; Terrones, M.; Crespi, V. H.; Alem, N. Defect Coupling and Sub-Angstrom Structural Distortions in $W_{1-x}Mo_xS_2$ Monolayers. *Nano Lett*. **2017**, 17, 2802−2808. DOI**:** 10.1021/acs.nanolett.6b05045.

[3] Ye, M.; Winslow, D.; Zhang, D.; Pandey, R.; Yap, Y. K. Recent advancement on the optical properties of two-dimensional molybdenum disulfide (MoS2) thin films. *Photonics* **2015**, 2, 288−307. DOI 10.3390/photonics2010288.

[4] Tonndorf, P.; Schmidt, R.; Böttger, P.; Zhang, X.; Börner, J.; Liebig, A.; Albrecht, M.; Kloc, C.; Gordan, O.; Zahn, D. R. T.; et al. Photoluminescence Emission and Raman Response of monolayer MoS_2, $MoSe_2$, and WSe_2. *Opt. Express* **2013**, 21, 4908–4916. DOI 10.1364/OE.21.004908.

[5] Mignuzzi, S.; Pollard, A. J.; Bonini, N.; Brennan, B.; Gilmore, I. S.; Pimenta, M. A.; Richards, D.; Roy, D. Effect of Disorder on Raman Scattering of Single-Layer MoS2. *Phys. Rev. B*: Condens. Matter Mater. Phys. **2015**, 91, 195411.

[6] Chung, D. Y.; Park, S. K.; Chung, Y. H.; Yu, S. H.; Lim, D. H.; Jung, N.; Ham, H. C.; Park, H. Y.; Piao, Y.; Yoo, S. J.; Sung, Y. E. Edge-Exposed MoS_2 Nano-Assembled Structures as Efficient Electrocatalysts for Hydrogen Evolution Reaction. *Nanoscale* **2014**, 6, 2131–2136, DOI 10.1039/C3NR05228A.

[7] Schutte, W. J.; De Boer, J. L.; Jellinek, F. Crystal Structures of Tungsten Disulfide and Diselenide. J.SOLID STATE CHEM. **1987**, 70, 207–209. DOI 10.1016/0022-4596(87)90057-0

[8] Walton, I. R.; Hibble, J. S. A combined *in situ* X-ray absorption spectroscopy and X-ray diffraction study of the thermal decomposition of ammonium tetrathiotungstate. *J. Mater. Chem.* **1999**, 9**,** 1347–1355. DOI: 10.1039/A900956F

[9] He, Q.; Wan, Y.; Jiang, H.; Wu, C.; Sun, Z.; Chen, S.; Zhou, Y.; Chen, H.; Liu, D. Haleem, Y. A. High-metallic-phase-concentration $Mo_{1-x}W_xS_2$ nanosheets with expanded interlayers as efficient electrocatalysts. *Nano Res.*, **2018**, 11, 1687−1698.

[10] Li, W.; Li, F.; Liu, Y.; Li, J.; Huo, H.; Li, R. Hydrothermal Synthesis of Multi-walled Carbon Nanotubes@$Mo_xW_{1-X}S_2$ hybrid as non-noble metal electrocatalyst for hydrogen evolution reaction. Int. J. Hydrogen Energy, **2017**, 42, 18774–18784.

[11] Gong, Q.; Cheng, L.; Liu, C.; Zhang, M.; Feng, Q.; Ye, H.; Zeng, M.; Xie, L.; Liu, Z.; Li, Y. Ultrathin MoS2(1−X)Se2X Alloy Nanoflakes for Electrocatalytic Hydrogen Evolution Reaction. *ACS Catal*. **2015**, 5, 2213−2219.

[12] Lin, Z.; Lin, B.; Wang, Z.; Chen, S.; Wang, C.; Dong, M. Gao, Q.; Shao, Q. Wu, S.; Ding, T; Liu H.; Guo, Z. Facile Preparation of 1T/2H-$Mo(S_{1-x}Se_x)_2$ Nanoparticles for Boosting Hydrogen Evolution Reaction. *Chemcatchem*, **2019**, 11, 2217–2222.